

Experimental and mechanistic description of merging and bouncing in head-on binary droplet collision

Kuo-Long Pan,¹ Chung K. Law,^{2,a)} and Biao Zhou²

¹*Department of Mechanical Engineering, National Taiwan University, Taipei 106, Taiwan*

²*Department of Mechanical and Aerospace Engineering, Princeton University, Princeton, New Jersey 08544, USA*

(Received 15 August 2007; accepted 4 December 2007; published online 17 March 2008)

The dynamics of head-on collision between two identical droplets was experimentally and computationally investigated, with emphasis on the transitions from merging to bouncing and to merging again, as the collision Weber number was increased. Experimentally the stroboscopically illuminated microphotographic images of two colliding droplet streams, generated through the ink-jet printing technique, were acquired with adequate temporal resolution of the collision event such that the instant at which the droplets merged for both soft and hard collisions was identified. Using this empirical information as an input, the simulated collision images were found to agree well with the experimental observations and allowed investigation of the collision flow field including the energy budget and the fundamental differences between the soft and hard collisions that lead to merging. It is further shown that the merging instant can be computationally assessed through the use of an augmented van der Waals force to effect merging through rupturing of the surfaces, with the associated Hamaker constant empirically but consistently extracted from the experimental observations. © 2008 American Institute of Physics. [DOI: 10.1063/1.2841055]

I. INTRODUCTION

Recent studies on binary droplet collision^{1,2} showed a nonmonotonic outcome in terms of merging and bouncing as the collision intensity is varied. For the limiting situation of head-on collision, four regimes of distinctively different outcomes with increasing collision Weber number, $We = 2\rho_\ell V_{\text{rel}}^2 R / \sigma$, were experimentally observed, where R is the droplet radius, V_{rel} is the relative velocity of the droplets, and ρ_ℓ and σ are the density and surface tension of the liquid, respectively. These four regimes are categorized according to (I) permanent coalescence after minor droplet deformation, (II) bouncing, (III) permanent coalescence after substantial droplet deformation, and (IV) coalescence followed by separation and the concomitant production of daughter droplets. Typical experimental and computed collision images for regimes I–III, which are the regimes of interest in the present study, are shown in Figs. 1–4 and will be studied in detail later. Experimental images for regime IV can be found in, for example, Refs. 1 and 3. Clearly, it is of both fundamental and practical interest to be able to describe the transition boundaries between these regimes. The transition between regimes III and IV has been successfully described in Ref. 2 by assessing whether the kinetic energy of the impact, plus the surface energy of the impacting droplets, can be adequately dissipated through the internal motion generated during impact, such that the remaining energy is just sufficient to constitute the surface energy of the spheroidized merged mass.

Phenomenologically, the propensity for bouncing or merging is a consequence of the readiness with which the gaseous mass in the interdroplet gap can be squeezed out of the gap by the colliding interfaces such that they can make

contact at the molecular level, leading to their destruction and thereby resulting in merging. The essential role of the interdroplet gaseous film has been experimentally demonstrated through the dependence of the collision outcome on the density of the gas medium.² Specifically, it was shown that increasing density by increasing either the pressure or molecular weight of the ambient gas promotes bouncing and widens regime II, while the opposite holds by reducing the density. Consequently, by progressively reducing the ambient pressure, regime II eventually vanishes. As such, it was found that regime II is eliminated for alkane droplets by steadily decreasing the ambient pressure from 1 to 0.6 atm. Similarly, while regime II does not exist for water droplets at 1 atm,^{1,4,5} it emerges as the system pressure is increased to 2.7 atm.²

Experimentally, studies on droplet collision have been primarily limited to the observation of the global collision images and the dependence of the collision outcome on the system parameters. Because of the small scale involved, it has not been possible to experimentally observe the dynamics of either the droplet internal motion or the gas motion within the interfacial gap. Consequently, computational simulation has been employed to gain understanding of the detailed collision dynamics. Notable efforts of this nature include those by Unverdi and Tryggvason⁶ and Nobari *et al.*,⁷ who used a front tracking method to trace the interface movement in a Lagrangian manner while treating the multiphase flow field as a unified domain and solving the governing equations on a grid of Eulerian coordinates. A similar study was conducted by Chin⁸ with a level set method. The evolution of the droplet surface geometry was computed, with substantial insight into the detailed properties of the flow field. Furthermore, the simulated droplet contour agrees

^{a)}Electronic mail: cklaw@princeton.edu.

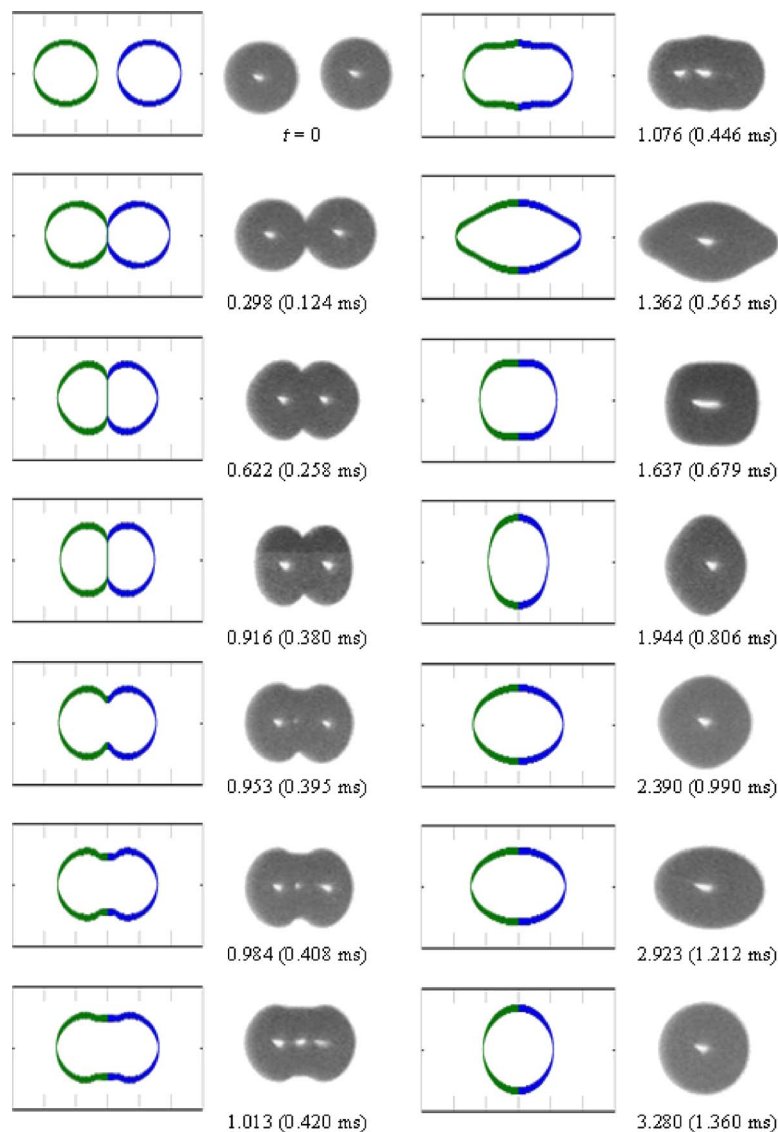


FIG. 1. (Color online) Merging collision sequence (in regime I) near the soft transition boundary ($We_s = 2.26$) determined by computation (left) and experiment (right). Conditions: Tetradecane in 1 atm air, $R = 107.2 \mu\text{m}$, $V_0 = 0.305 \text{ m/s}$, $We = 2.25$, and $T = 0.415 \text{ ms}$.

well with the experimental images for bouncing collisions. A comparison for merging collisions, however, has proven to be ambiguous because of lack of description for the merging of the colliding interfaces. Fundamentally, since the numerical simulation was based on continuum mechanics while the final stage of the interfacial dynamics leading to merging must necessarily involve molecular forces and thereby also rarified flow, lack of such basic information in the computational model renders it unfeasible to simulate the rupture of the interfaces from first principles. This difficulty was circumvented by artificially, and quite arbitrarily, removing the interfaces at a certain instant when they are sufficiently close to each other. The fidelity of the simulation then depends on the instant at which rupture is implemented, and it was also found^{7,8} that the simulated dynamics depends very sensitively on the specification of this instant.

The present study was motivated by our experimental observation that the occurrence and instant of merging could be identified through a distinct change in the contour of the imaged interface and the recognition that such an instant could be time resolved with sufficient accuracy such that, by using it as an input to the computational simulation based on

continuum mechanics, the evolution of the experimental collision images subsequent to merging can be satisfactorily simulated. Investigations related to this effort will be presented first.

Having established the adequacy of this empirically enabled computational simulation approach, we shall study the various issues related to the merging and bouncing aspects of the collision dynamics, including the energy budget, the flow field characteristics, and the evolution of the geometry and dynamics of the interfacial gap. The emphases are on the transition between bouncing and merging regimes and the differences between the transitions from regimes I to II, and II to III, which we shall designate, respectively, as soft and hard collisions. The role of the van der Waals force in effecting merging is also investigated.

II. FORMULATION AND NUMERICAL SPECIFICATION

The front tracking method adopted herein was developed by Unverdi⁹ and discussed by Unverdi and Tryggvason.⁶ The computational code is an axisymmetric version of the method, described by Nobari *et al.*⁷ The droplets are initially

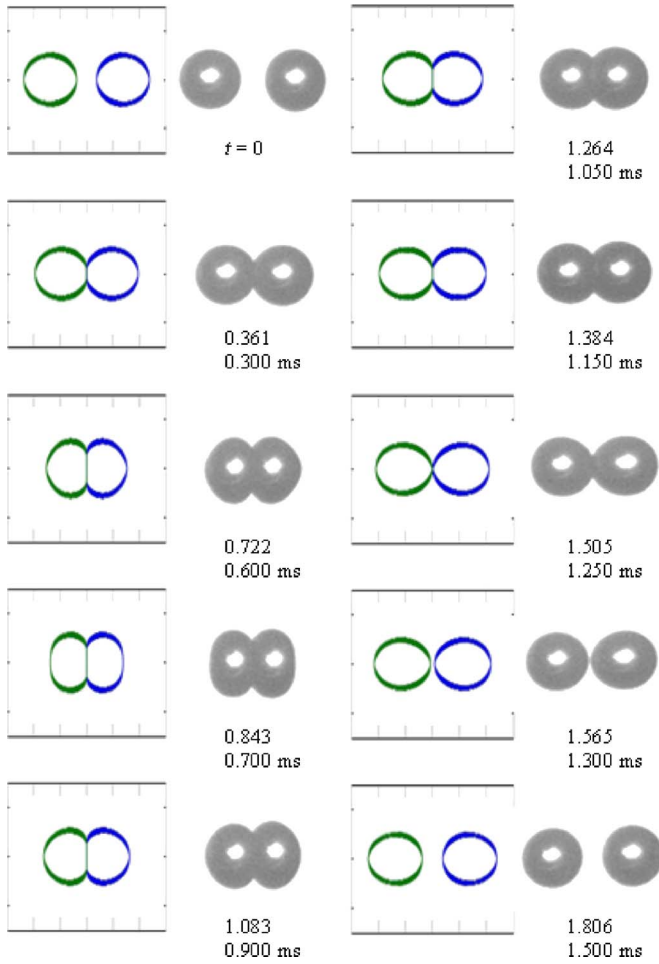


FIG. 2. (Color online) Bouncing collision sequence (in regime II) near the soft transition boundary ($We_s=2.26$) determined by computation (left) and experiment (right). Conditions: Tetradecane in 1 atm air, $R=170.6 \mu\text{m}$, $V_0=0.243 \text{ m/s}$, $We=2.27$, and $T=0.831 \text{ ms}$.

placed at each end of the z axis with an experimentally prescribed distance z_0 . The Navier–Stokes equations are solved for both gas and liquid phases in a unified domain:

$$\frac{\partial(\rho\mathbf{V})}{\partial t} + \nabla \cdot (\rho\mathbf{V}\mathbf{V}) = -\nabla p + \rho\mathbf{g} + \nabla \cdot \frac{1}{\text{Re}}(\nabla\mathbf{V} + \nabla\mathbf{V}^T) - \frac{8}{\text{We}} \int_{\Delta_s} \kappa \mathbf{n} \delta(\mathbf{r} - \mathbf{r}_f) da, \quad (1)$$

where \mathbf{V} , ρ , and p are the velocity, density, and pressure, respectively, normalized by the initial droplet velocity V_0 given by $2V_0=V_{\text{rel}}$ for identical droplets, liquid density ρ_ℓ , and the dynamic pressure $\rho_\ell V_0^2$, and t is time normalized by R/V_0 . The Reynolds number Re is defined as $\rho_\ell V_0 R/\mu$, where μ is the viscosity. In Eq. (1) the surface tension is added as a delta function integrated locally over the immiscible interface within unit volume in order to render a singular force exerted by the droplet and is calculated over the entire droplet surface. Furthermore, $\rho\mathbf{g}$ is a body force that is turned off at a prescribed droplet separation before collision and is merely used to provide the droplet with an initial velocity with the solved velocity field of the surrounding gas.⁷ The notations for volume and surface are for three dimensions but we have used their two-dimensional versions,

i.e., surface and line. Here κ is twice the mean curvature, \mathbf{n} the outwardly directed unit normal vector at the droplet surface, and \mathbf{r} the space vector with the subscript f designating the interface.

In the computation the grid lines are unevenly spaced, with a minimum spacing of 0.002 at the center plane of collision, and only a quarter of the domain is simulated because of symmetry. The distance between gridlines increases smoothly as it moves away from the center plane. It is also noted that the dimension of the interfacial gap is only about $O(10^{-3})$ that of the droplet size, indicating the substantial disparity in the relevant physical scales of the phenomena and the gentleness of the interfacial curvature developed upon collision.

Details of the numerical approach, settings, and validation of convergence can be found in Refs. 10 and 11.

III. EXPERIMENTAL SPECIFICATIONS

The experimental apparatus and procedure are those of Jiang *et al.*¹ and Qian and Law.² Here two identical nozzle-generated streams of droplets of uniform size were made to impinge onto each other. Time-resolved images were taken through stroboscopy synchronized with the droplet generation circuit, whose resolution was about $5 \mu\text{s}$. However, due to the unavoidable unsteadiness in droplet generation, the actual temporal resolution was about $15 \mu\text{s}$. A digital imaging system then accurately time resolved the collision event, recorded the droplet image, and processed the data. This yielded the fine temporal resolution of the transitional behavior between different regimes and is critical in determining the instant of rupture of the interfacial gas film. The entire apparatus was housed in a chamber whose pressure can be varied between 0.1 and 20 atm. Only head-on collision events were studied. Most of the investigations were conducted using n -tetradecane.

IV. GLOBAL COLLISION DYNAMICS

In this section the experimental and computational collision images of tetradecane droplets in 1 atm pressure are compared, emphasizing the phenomena of merging and bouncing around the transitional boundaries of soft and hard collisions.

A. Experimental and simulated images of bouncing and merging

Figures 1 and 2 show the experimental and computed droplet collision sequences illustrating the soft transition from merging to bouncing with increasing Weber number, while Figs. 3 and 4 illustrate the hard transition sequences, from bouncing to merging. In the following discussion, t is time normalized by the droplet oscillation period, $T=2\pi(\rho_\ell R^3/8\sigma)^{1/2}$, based on inviscid droplet oscillation with small amplitude.¹² The real time is indicated in the figures as well.

Figure 2 shows that, for the bouncing case, the simulation agrees well with the experimental data in terms of matching the overall deformed droplet configuration and collision phase. For the merging case (Fig. 1), it was found that,

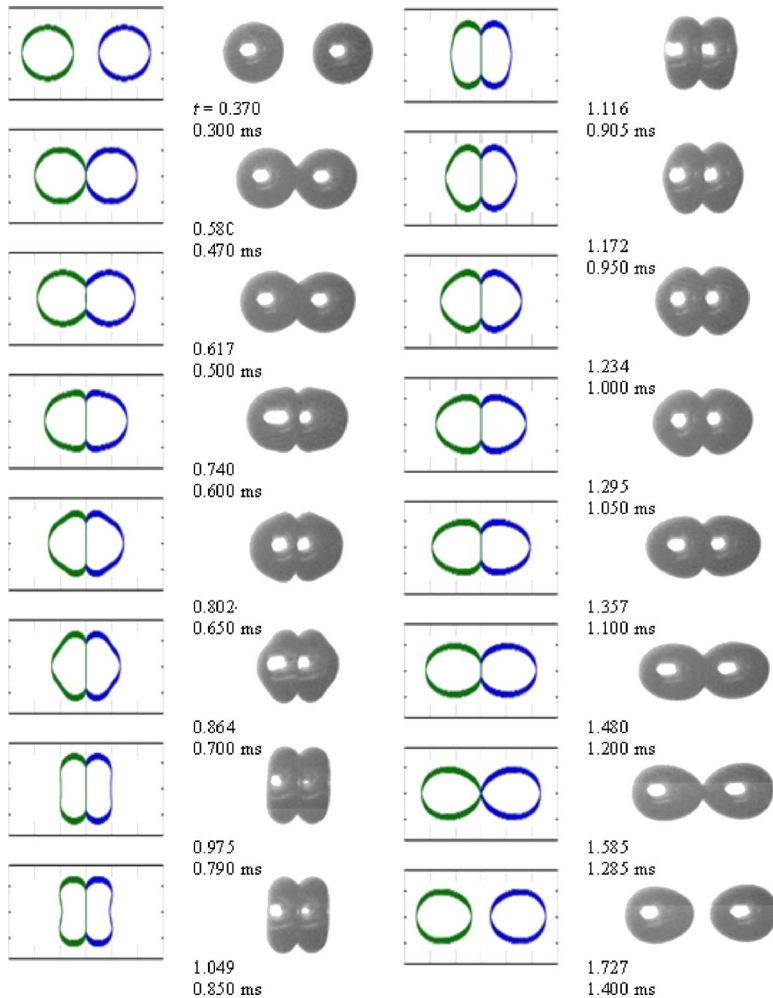


FIG. 3. (Color online) Bouncing collision sequence (in regime II) near the hard transition boundary ($We_H = 12.3$) determined by computation (left) and experiment (right). Conditions: Tetradecane in 1 atm air, $R = 167.6 \mu\text{m}$, $V_0 = 0.496 \text{ m/s}$, $We = 9.33$, and $T = 0.811 \text{ ms}$.

by gradually adjusting the synchronization time between droplet generation and strobe lighting, there exists a narrow range in time over which the cuspy contour between the two droplets abruptly becomes smooth, as shown for the consecutive images obtained at the instants of $t = 0.916$ and 0.953 , corresponding to a physical duration of about $15 \mu\text{s}$, which is the resolution of the collision instant. Using the average of these consecutive times ($t = 0.935$) as the instant of surface rupture, at which the impinging interfaces separating the liquid and gas phases are removed, the computed sequence of collision images of Fig. 1 shows very close agreement with the experimental sequence. Furthermore, the state of merging is seen to take place around that of maximum deformation, within the resolution of the images shown. We shall show in due course that merging actually occurs slightly beyond the attainment of maximum deformation.

To demonstrate the sensitivity of the computed dynamics on the timing of the rupture of the interfaces, Figs. 5(a) and 5(b) show, respectively, the computed evolutions subsequent to an earlier ($\Delta t = -0.078$) and a later rupture ($\Delta t = 0.151$) for the sequence of Fig. 1. The comparison shows substantial differences between the computational and experimental phases in that earlier and later rupturings generate, respectively, leading and lagging phases.

When We is increased to the hard collision transition boundary, We_H , the collision outcome changes from bounc-

ing to merging, as shown in Figs. 3 and 4, respectively. In Fig. 4, the experimental time for rupture, as defined by the smoothing of the interface cusp, was found to be 0.446 (0.368 ms). By using this value as the rupture time, good comparison between the computed and experimental results is again observed. It is also noted that merging in this case of hard collision occurs as the deformed droplet is flattened to a disk shape while the incoming mass at the center of the rear face is still heading forward, as shown for the time interval of $t = 0.443$ and 0.545 in Fig. 4. This behavior is distinctively different from that of regime I in which the breakup of the interfaces occurs subsequent to the attainment of the maximum deformation and the droplets have started to retract. Thus although the forward motion of the rear face of the droplet could not be experimentally imaged at $t = 0.545$ and 0.606 as they were obscured by the annular rim, the indented shape of the droplet was captured by the computation.

The above results therefore support the adequacy and accuracy of the computational simulation, the suggestion of identifying the instant of rupture by that of the change in the interface contour, and the feasibility of using this instant to simulate the global collision event with merging.

Having established the fidelity of the present empirically enabled simulation of the collision dynamics, we shall study in the following various issues related to bouncing and merging in droplet collision.

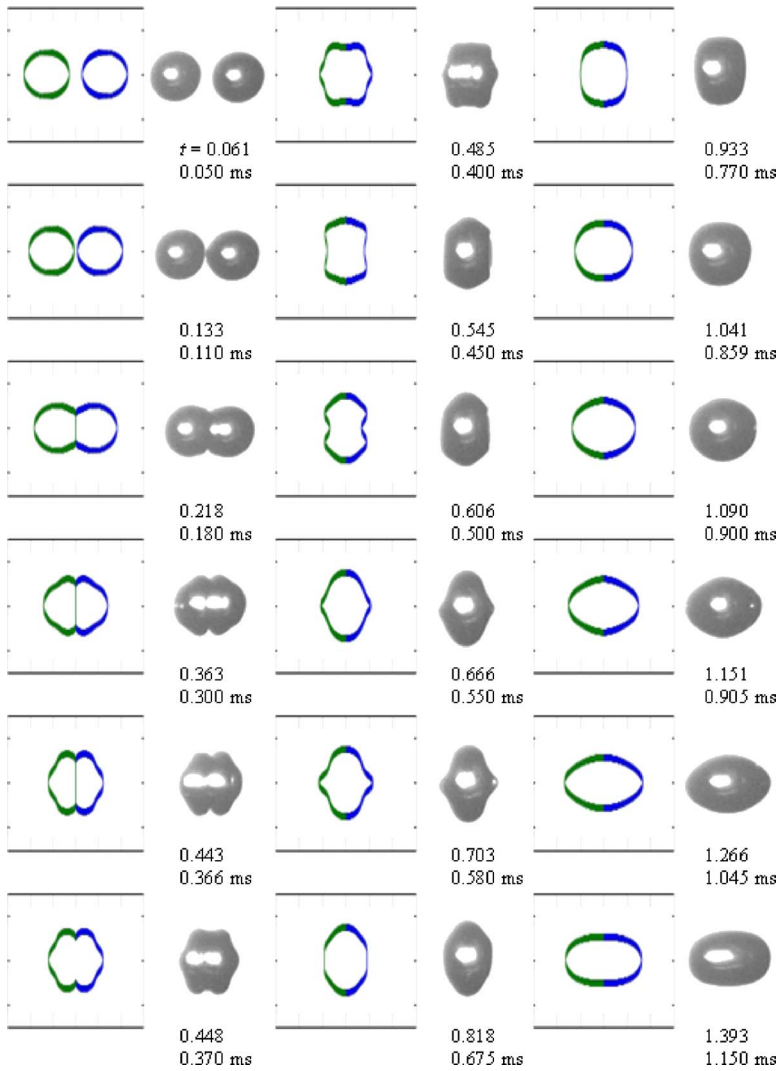


FIG. 4. (Color online) Merging collision sequence (in regime III) near the hard transition boundary ($We_H = 12.3$) determined by computation (left) and experiment (right). Conditions: Tetradecane in 1 atm air, $R = 169.7 \mu\text{m}$, $V_0 = 0.596 \text{ m/s}$, $We = 13.63$, and $T = 0.826 \text{ ms}$.

B. Evolution of the energy budget

The total energy of the flow field consists of surface energy, kinetic energy, and the cumulative viscous dissipation energy. Since the energy conservation equation was not solved in the simulation, these energy components were evaluated through the velocity and density fields as well as the surface geometry. For example, the viscous dissipation rate, given by¹³

$$\Phi = \mu \left[2 \left(\frac{\partial u}{\partial r} \right)^2 + 2 \left(\frac{u}{r} \right)^2 + 2 \left(\frac{\partial w}{\partial z} \right)^2 \right] + \mu \left(\frac{\partial u}{\partial z} + \frac{\partial w}{\partial r} \right)^2 - \frac{2}{3} \mu \left[\frac{1}{r} \frac{\partial(ru)}{\partial r} + \frac{\partial w}{\partial z} \right]^2, \quad (2)$$

consists of three sources that represent, respectively, effects due to the normal strain, the shear strain, and volumetric dilatation, with the last being much smaller than the other two due to incompressibility. At the state of merging, all surfaces interior to the circumference of the cusp are removed, with the associated surface energy implicitly assumed to be either dissipated thermally or stored as surface energy of small, secondary drops that may form when the interstitial gap is ruptured.⁷

The evolution of the various energies of the colliding droplets corresponding to the bouncing and merging cases of Figs. 2 and 1 are shown in Figs. 6 and 7, respectively. For the bouncing case of Fig. 6, it is seen that although energy conservation is not explicitly included in the numerical scheme, the total energy, obtained by summing the accumulated dissipation loss with the surface and kinetic energies, is conserved. This indicates that the velocity field and the surface geometry are resolved well. The results show that the state of the largest deformation, at $t = 0.843$, is characterized by the maximum surface energy and minimum kinetic energy. Viscous dissipation, as indicated by the viscous dissipation rate, is initiated at an early stage, around the instant of contact when the kinetic energy starts to decrease and before significant deformation. Furthermore, since the surface energy of the bouncing case remains unchanged from the initial value after the droplet has resumed its spherical shape, the loss of KE is completely converted to DE.

For the merging case of Fig. 7, since a certain amount of the interfacial surface area is removed at the instant of merging, surface energy, and hence the total energy, is reduced abruptly after the numerical rupture. It is seen that rupturing occurs shortly after the colliding mass has achieved its maximum deformation, with the surface energy attaining its cor-

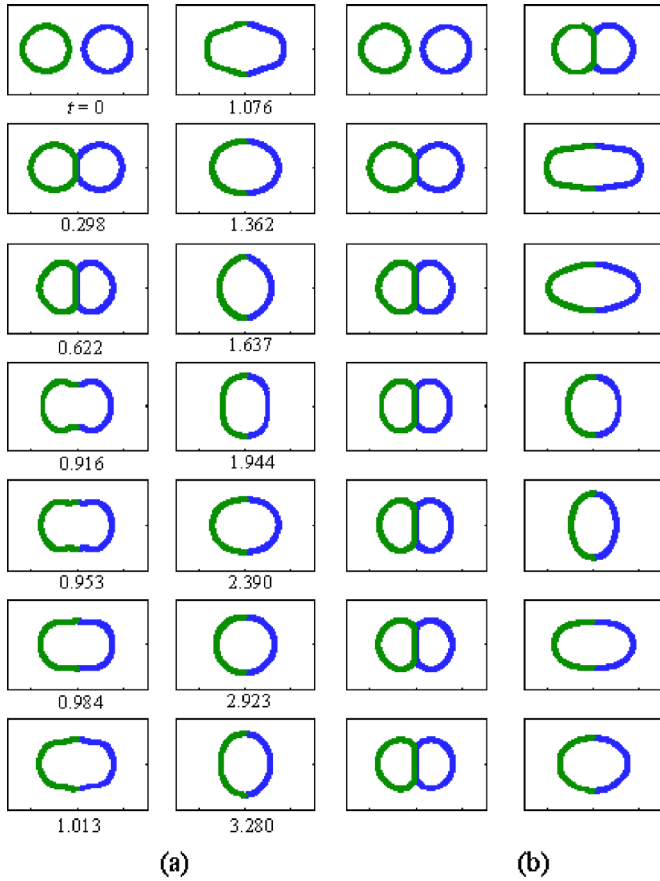


FIG. 5. (Color online) Computed merging collision sequences near the soft transition boundary for the experimental sequence of Fig. 1 assuming slightly (a) earlier ($\Delta t = -0.078$) and (b) delayed ($\Delta t = 0.151$) merging instants, demonstrating the sensitivity of the collision event to the instant of merging.

responding maximum value. Furthermore, upon rupture, a spike in the viscous dissipation rate is generated, which in turn contributes to a rapid increase of the cumulative dissipation energy. This spike results from the perturbation of the local flow field due to the sudden connection of the interfaces. It is further seen that, subsequent to merging, the merged mass undergoes oscillation, leading to additional viscous energy loss.

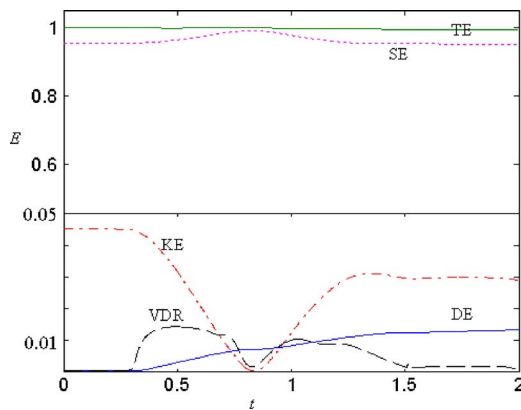


FIG. 6. (Color online) Energy components of the colliding droplets vs time near We_s for bouncing ($We = 2.27$). Legend: KE is total kinetic energy, DE is total dissipation energy, SE is surface energy of the drop, TE is total energy, and VDR is viscous dissipation rate multiplied by unit time, each normalized by the initial energy of a single droplet.

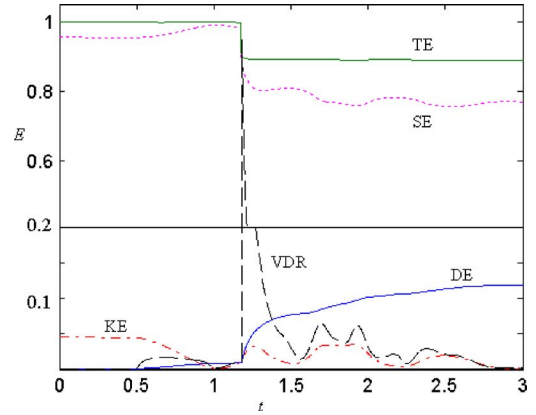


FIG. 7. (Color online) Energy components of the colliding droplets vs time near We_s for merging ($We = 2.25$). Same legend as that of Fig. 6.

For the bouncing case with We larger than that of Fig. 6 but smaller than $We_H (= 12.3)$, Fig. 8 shows that since the collision is now more energetic, the relative amount of the kinetic energy is increased while the surface energy is reduced. Furthermore, the substantial distortion of the droplet results in a relatively large dissipation, while the kinetic energy is greatly reduced after collision because of the substantial viscous energy loss.

For the merging case at a higher $We (= 13.63)$, around We_H , Fig. 9 shows the reduction of surface energy at the instant of merging, leading to a strong dissipation rate in the same manner as that of Fig. 7. The merging, however, occurs at an earlier phase of the collision as compared to the soft collision case of Fig. 7 because of the stronger impact inertia. Furthermore, there is also a second spike of the dissipation rate, caused by oscillation of the merged mass. This leads to a further dissipation of the kinetic energy such that the merged mass would be able to contain all the energy through its surface tension and remain as a single, spherical entity.

In summary, comparing the merging outcomes for the soft and hard collisions (Figs. 7 and 9), it is found that in terms of the fractional distribution of the various forms of energy, soft collision has relatively small kinetic energy and large surface energy. It also suffers less distortion and hence less dissipative loss. Merging through hard collision, how-

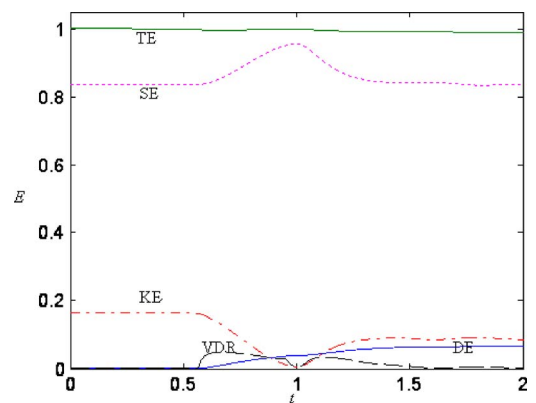


FIG. 8. (Color online) Energy components of the colliding droplets vs time near We_H for bouncing ($We = 9.33$). Same legend as that for Fig. 6.

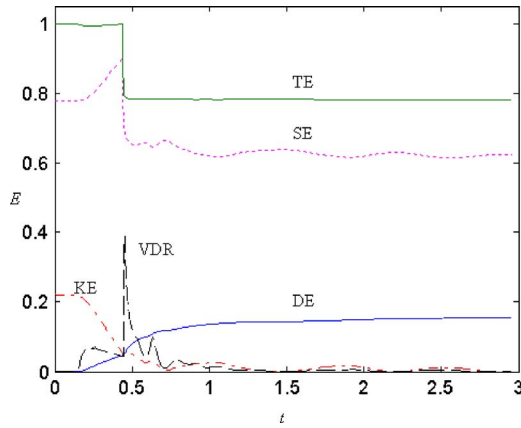


FIG. 9. (Color online) Energy components of the colliding droplets vs time near We_H for merging ($We=13.63$). Same legend as that for Fig. 6.

ever, suffers more loss in the mechanical energy, which is composed of both surface and kinetic energies. This is because hard collision has relatively more kinetic energy, which is eventually transformed to surface energy through substantial deformation during and after contact. Consequently by removing the interface upon merging, a relatively large amount of energy is lost as well. It is also seen that evolution of the dissipation rate is similar to that of kinetic energy, which attains a local maximum as the surface energy is minimized with the spherical shape restored.

C. Spatial distribution of flow properties

Further insight into the dynamics of soft versus hard collisions can be gained by examining the spatial profiles of pressure, velocity, and viscous dissipation.¹⁰ These results show that for the soft bouncing situations, there is strong dissipation around the opening of the gas film at the early and late phases when the droplet is about to deform and to recover its spherical shape, respectively. By analyzing each component of the motion, it is found that the shear strain contributes predominantly to the viscous dissipation. Furthermore, the distribution of the velocity vectors indicates that the flow is turned sharply outward in the radial direction as the interfaces approach each other and squeeze the intervening gas out of the interfacial gap [$t=0.361$, Fig. 10(a)], and is turned sharply inward as they rebound and entrain the surrounding gas into the interfacial gap [$t=1.505$, Fig.

10(b)]. Therefore, there exists a high pressure source in the gas film during the approaching period and a low pressure sink during the receding period.

In addition to the gas phase, dissipation also occurs within the droplet, caused by the compression induced by the forward motion of the rear part of the droplet, as well as around the waist of the deformed droplet as a result of the recirculation of the surrounding gas. These dissipation sources, however, are extremely small relative to the total energy. This is physically reasonable because soft collision associated with small kinetic energy leads to small and slow deformation, resulting in weak strain rates in the liquid.

If the approaching interfaces are ruptured as We is slightly reduced from We_S , the development before the onset of merging is similar to that of bouncing, although the subsequent dynamics is quite different, as shown in Fig. 11. Specifically, before rupturing, the surrounding gas is already entrained into the interfacial gap [Fig. 11(a)] and dissipation is generated at its opening to the ambience. Immediately after rupturing, the connected interfaces with negative curvature contract rapidly due to surface tension and strong recirculation is produced as depicted by the velocity vectors in Fig. 11(b). This then leads to a high dissipation rate around the region of connection, and consequently a substantial increase in the global dissipation rate, as shown in Fig. 7. This region expands outward along the droplet surface, being pulled by the surface tension exerted at the expanding rim of the merged interface. The subsequent evolution is governed by the velocity and pressure fields balanced with the surface tension, resulting in prolonged and contracted oscillations whose periodicity is of the order of the natural oscillation time, as shown in Fig. 7.

For bouncing at higher We close to We_H , the droplet spreads out into a disk shape due to its larger impact inertia. The dissipation loss is caused not only by the squeezed gas during the approaching and receding phases in the same manner as that for soft collision but also by the strained liquid as the droplet is deformed. However, while dissipation in the gas in soft bouncing is about 14% of that in the liquid, it becomes much smaller in hard collisions. This is due to the fact that substantial dissipation is present in the liquid for a longer time while in the gas, it exists only for a short period in a small region when the interdroplet gap is greatly squeezed. The present result therefore confirms the previous

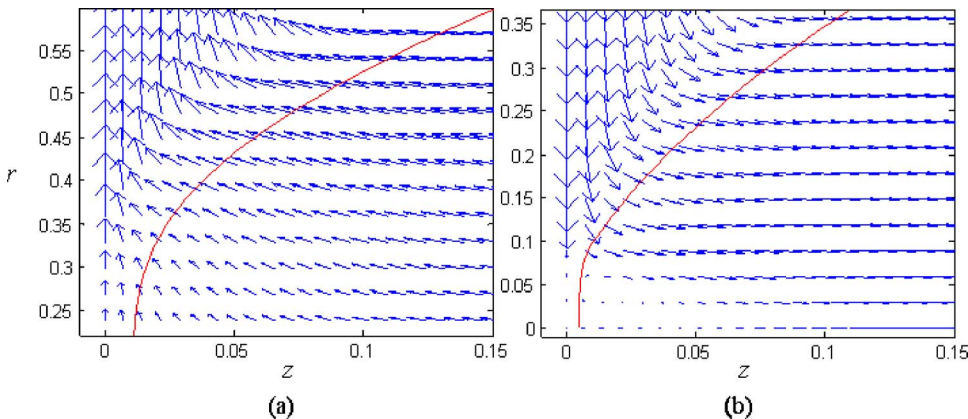


FIG. 10. (Color online) Distribution of velocity vectors at (a) $t=0.361$ and (b) $t=1.505$ for the bouncing case near We_S ($We=2.27$).

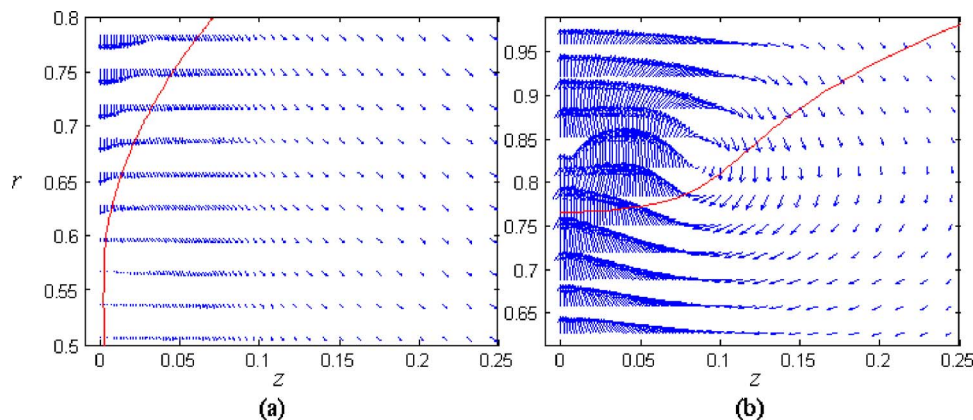


FIG. 11. (Color online) Distribution of velocity vectors at (a) $t=0.916$ and (b) $t=0.953$ for the merging case near We_S ($We=2.25$).

assumption^{1,2} that viscous dissipation is negligible in the gas phase for collisions with large deformation. The region of high dissipation rate starts from the waist when the impinging liquid flow is turned outward in the radial direction ($t=0.580$). It is then swept along the droplet surface toward the indentation at the rear portion where the incoming flow motion is stopped, when t is slightly smaller than 1.049, as shown in Fig. 3.

The flow structure for the merging collision with We slightly larger than We_H is similar to that of regime I in that immediately after rupture of the interfaces, the ensuing mixing of the flow induces recirculation due to the outward motion of the connected surface segment, which leads to a strong strain rate ($t=0.485$) and a period of substantial viscous loss, and thus generates the first spike shown in Fig. 9. The second spike in the dissipation rate occurs at $t \approx 0.635$ and is caused by the oscillating dimple of the deformed droplet, which lasts about 1 cycle as seen in the sequential images in Fig. 4, from $t=0.448$ when the liquid flow is impinging until $t=0.703$ when the flow is returned and an ejected bulge is formed. The contracting and protruding phases of the oscillating surface correspond to two local maxima of the surface energy as shown in the evolution of the energy budget (Fig. 9, $t \approx 0.585$ and 0.715 , where a local minimum between them represents the neutral position of the oscillation). This is a consequence of the balance between the impinging inertia and surface tension, which induces a high strain rate and hence substantial dissipation. Specifically, the local pressure minimum at the surface indentation indicates a sink caused by the substantial deformation and negative curvature, which then entrains the liquid at the sides. Consequently a growing bulge is generated at the center, similar to that of the bouncing case. Because of merging, however, this bulge is now pulled back, as shown at $t=0.703$, and moves outward in the radial direction due to expansion of the merged interface ($t=0.818$). It ends in an oscillatory motion that is analogous to the natural oscillation of a spherical droplet.

V. DYNAMICS OF THE GAP CONTOUR

The following discussion is based on the shape and minimum separation distance between the droplet interfaces.

A. Evolution of the gap contour

Figure 12 shows the temporal variation of the shape of half of the interfacial gap, $h(r)$, during collision, with $We=2.26$. It is seen that as the interface approaches the symmetry plane, the high pressure buildup in the direction of the lines connecting the centers causes indentation on the droplet surface such that the minimum clearance takes the form of a ring concentric along the line of centers. Such “dimples” are well-established phenomena and have been extensively observed during the drainage of axisymmetric films.¹⁴ We also note that the appearance of the severity of the curvature of the interface in the present plots is greatly exaggerated due to the significant disparity between the radial and axial scales.

It is further seen that as the droplet surface approaches the maximum deformation with increasing flattening of its global shape, the indentation in the center increases while the size of the minimum clearance ring expands. After the droplet has reached its maximum deformation at $t=0.91$, most of the initial droplet kinetic energy is transformed into the surface tension energy. At this stage, the droplet starts to contract due to surface tension and rebound by the contracting flow inside. This is depicted by the dashed lines, which show the gap evolution for $t > 0.91$ after the droplet has reached maximum deformation. As the droplet bounces away, relief of the pressure in the gas gap causes the radius of the clearance ring to decrease and the gap to widen. Then between $t=1.45$ and 1.50 , a positive pressure difference is generated

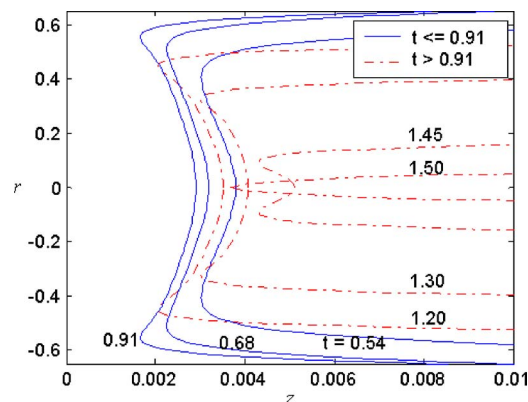


FIG. 12. (Color online) Evolution of interdroplet gap geometry for tetradecane in 1 atm air with $We=2.26$ ($R=170.6 \mu\text{m}$, $V_0=0.243 \text{ m/s}$, and $T=0.831 \text{ ms}$).

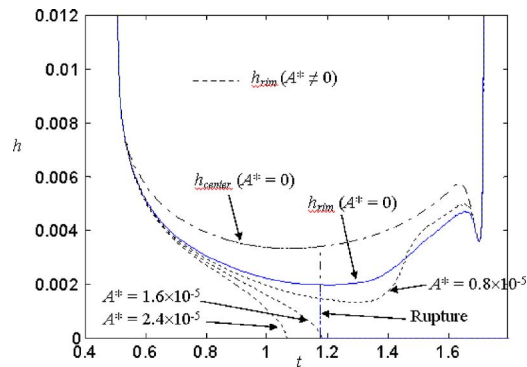


FIG. 13. (Color online) Evolution of h_{center} and h_{rim} for soft tetradecane droplet collision with merging in 1 atm air for $We=2.26$ ($A^*=0$). The h_{rim} associated with the augmented van der Waals force are also shown, for which $A^* \neq 0$.

by the higher pressure within the liquid and the lower pressure in the gas gap, causing the indented surface to “buckle” rapidly. This renders the minimum clearance position to switch back from the rim to the center, resulting in an abrupt reduction in the effective minimum gap width even as the interfaces are receding from each other globally.

B. The role of the minimum gap width

To further investigate the propensity of bouncing versus merging with respect to the width of the gas gap, we have tracked the evolution of the interface boundary for the merged states around the soft (Fig. 13) and hard (Fig. 14) transition boundaries (for $A^*=0$, A^* is to be introduced later) by plotting the center clearance, h_{center} , and the minimum gap clearance at the rim, h_{rim} , as functions of time. The instants of merging were noted from the experiments but were not implemented in the simulation so that h_{rim} and h_{center} are shown in order to provide an indication of their movements. It is seen that, in general, during most of the collision event, the indentation is present causing $h_{\text{center}} > h_{\text{rim}}$, while during the initial and final stages, the reverse holds, with h_{center} representing the minimum distance when the indentation is absent. Buckling of the indentation is clearly completed beyond the state of the second minimum.

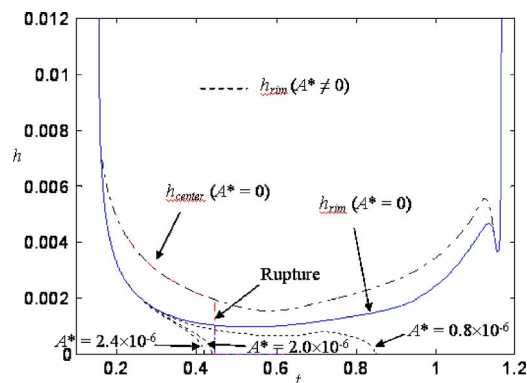


FIG. 14. (Color online) Evolution of h_{center} and h_{rim} for hard tetradecane droplet collision with merging in 1 atm air for $We=13.63$ ($A^*=0$). The h_{rim} associated with the augmented van der Waals force are also shown, for which $A^* \neq 0$.

Using the experimental rupture time as a marker, it is seen that rupturing of the impinging surfaces for the soft collision occurs after the interfaces have reached the shortest separation distance and the center of the indentation (h_{center}) has started to recede from each other, while rupturing for the hard collision occurs before the gap of the rim has reached its minimum value. Thus while merging may have occurred at the rim for both soft and hard collisions, it takes place during the receding and approaching phases of the interface motion, respectively. This result is consistent with the experimental observations and the computed flow fields and energy budgets noted earlier.

Anticipating the dominance of the intermolecular attraction force during the last stage of the merging process, we next study the dynamics of the gap contour with the presence of such a force.

VI. DYNAMICS OF MERGING

A. Simulation of merging with augmented van der Waals force

To attempt a simulation of the interface merging with molecular force, we first note that the calculated minimum gap distance for collisions resulting in merging is about $0.2 \mu\text{m}$, which is an order of magnitude larger than the range for the van der Waals force to be effective. Thus some essential physics is missing in the simulation, which will be discussed later. It is, however, reasonable to conduct a simulation by artificially increasing the magnitude of the van der Waals force, with the extent of augmentation determined by the empirical state of merging. Through such a simulation, the characteristics of the merging dynamics due to molecular attraction can be assessed.

The influence of the van der Waals force can be incorporated in the formulation by adding a “negative” pressure at the droplet surface, i.e., $A/(6\pi\delta^3)$, where A is a coefficient and δ the interdroplet separation. It is treated as a surface force and is smoothed out by means of the immersed technique in the same manner as that for the surface tension. This attractive force, which is inversely proportional to the cubic power of the separation distance of the interface, was derived based on two flat plates with semi-infinite extent.¹⁵ This configuration is justified for the present situations in that the surface at the closest approach of the rim does locally approach a flat shape, with the axial variation of the front position being about two to three orders smaller than that in the radial direction. Since the attraction is extremely sensitive to the interdroplet separation, its influence prevails around the rim which has the shortest separation distance. We are interested in assessing if force of this nature can provide sufficient attraction to effect merging.

Using $A^*=A/(\rho_\ell V_0^2 R^3)=1.6 \times 10^{-5}$, Fig. 15 shows that the interface, especially that at the rim, now accelerates toward the symmetry plane. This is further demonstrated in Figs. 13 and 14, in which the accelerative temporal variation of the h_{rim} is shown. In the simulation, if the interfaces were not manually removed when they became very close, the computation would eventually diverge, indicating the onset of merging. Asymptotic theories that assume certain limit

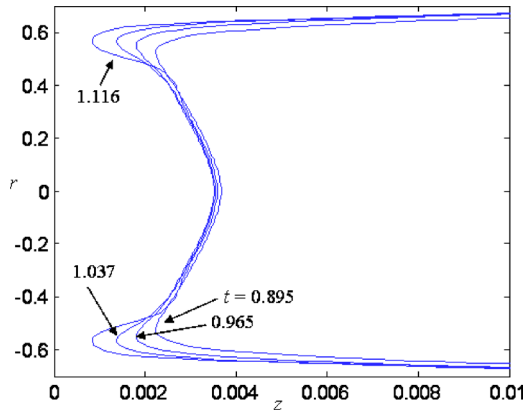


FIG. 15. (Color online) Accelerating surface movement in the presence of augmented van der Waals force; $A^* = 1.6 \times 10^{-5}$ (soft tetradecane droplet collision in 1 atm air for $We = 2.26$).

conditions such as small We we have also predicted similar evolution of the droplet surface before rupturing.¹⁶ It was thus determined that, to effect merging, the dimensionless force coefficient A^* falls within the range of 10^{-6} – 10^{-5} , which corresponds to A being about 10^{-15} J. It was further found that the occurrence of the attractive movement is sensitively affected by the value of A . For example, Fig. 13 shows that while $A^* = 0.8 \times 10^{-5}$ fails to bring the surfaces close enough for merging to occur, merging is effected by using a slightly larger value of 2.4×10^{-5} . Narrowing A^* to 1.6×10^{-5} ($A = 1.39 \times 10^{-15}$ J) then results in merging at the experimentally observed instant. Similarly, for the hard collision situation of Fig. 14, a value of 2.0×10^{-6} for A^* ($A = 2.65 \times 10^{-15}$ J) was found to reproduce the experimentally observed merging time.

In reality, $A = \pi^2 q^2 \lambda$ is the Hamaker constant and is determined by the atomic density (q) and London–van der Waals constant of the interacting materials (λ), with modified effects of the immersion fluid.¹⁵ It is always positive for particles of the same material and thus generates attraction. The magnitude of A is generally between 10^{-21} and 10^{-18} J and is about 5.0×10^{-20} J for liquid tetradecane in vacuum.

Since the force coefficients used in effecting merging in Figs. 13 and 14 are of the order of 10^{-15} J, which is substantially larger than the Hamaker constant of 10^{-21} – 10^{-18} J, the approach distance is too large for the van der Waals force to be effective as anticipated earlier. However, if the interface separation distance is one order smaller, e.g., changing from 0.2 to 0.01 μm , and since the attractive force varies inversely with the cubic power of the separation distance, our calculated coefficient A would fall in the range for the intermolecular force to take substantial effect. The result therefore is consistent and substantiates the merit of using the augmented Hamaker constant to investigate the merging dynamics.

The above results also indicate that some other factors could be present and would have allowed the interfaces to approach each other closer than calculated, thereby effecting the observed merging. These are discussed next.

B. Additional factors affecting merging

Since the characteristic dimension of the interdroplet film is close to that of the rarified gas regime, which is about 0.1 μm at atmospheric condition, the Knudsen number, representing the ratio of mean free path to the characteristic length, is an $O(1)$ quantity. It is therefore reasonable to suggest that a proper rarified gas treatment would have resulted in a lower pressure within the gap, which would have allowed the interfaces to approach each other closer and subsequently trigger the molecular attractive force. Indeed, investigations of this nature have been conducted analytically for solid particles with small deformation in collision by Hocking,¹⁷ Barnocky and Davis,¹⁸ and Sundararajakumar and Koch.¹⁹ By implementing the Maxwell slip boundary condition or solving the linearized Boltzmann equation, it was found that when the interparticle gas gap becomes as small as the mean free path or less, the mass flux drained out is modified and the resistant force in the lubrication layer is reduced as compared to that predicted based on continuum mechanics. Consequently the singularity of the lubrication force as the film thickness approaches zero, which results from the inverse proportionality between the repulsive force and gap thickness, is avoided and the particles are able to make contact.

Another possible factor that restrains the interfaces from moving toward each other is the neglect of compressibility during collision, which excludes the variation of density with pressure. This effect has been studied in particle collisions by asymptotic analyses.^{20–22} Since the gas is squeezed as the gap becomes small, the pressure, as well as density, can be elevated substantially. Recognizing that the Reynolds number of the gas flow in the gap is $O(1)$,^{2,23} the inertial and viscous terms are of equal significance in balancing the driving pressure. By equating $(\partial p / \partial r) \sim 2\mu_g(\partial^2 u / \partial z^2)$, where u is the radial velocity and μ_g is the gas viscosity, and by using mass conservation, $V_0 \sqrt{Rh} \sim uh$, based on characteristic dimensions of $(Rh)^{1/2}$ and h for r and z directions, respectively, and in an approximation assuming parabolic shape of the interface,^{21,24} the order of the pressure difference across the channel is found to be $2\mu_g V_0 R / h^2$. If this term is comparable to the pressure of the ambient gas p_0 , i.e., the separation distance is at $h_{\text{comp}} \sim (2\mu_g V_0 R / p_0)^{1/2}$, compressibility will then play a significant role in the drainage such that the density change needs to be considered in mass conservation.²² These previous analytical studies showed that compressible effects could reduce the lubrication force in the gas gap as compared to the incompressible results and hence promote the propensity for particles to come closer. In the current condition, h_{comp} is of the order of 0.1 μm and thus compressibility could also have lowered the pressure in the gap, leading to a closer approach.

VII. CONCLUDING REMARKS

In the present investigation, we have experimentally and computationally studied the head-on collision dynamics of two impinging droplets. The crucial factor responsible for the success of the present study is the ability to experimentally identify and resolve the instant of merging, at which the

cuspy curvature of the unmerged interfaces suddenly smoothens. Using this empirically supplied information in the computational simulation, the various aspects of the droplet collision dynamics, especially those associated with merging, were satisfactorily simulated with confidence. Analysis of the evolution of the energy budget shows that viscous loss in the gas phase is substantially smaller than that in the droplet, especially for hard collisions, thereby justifying the previous assumption¹ of negligible gas-phase dissipation situations involving hard collisions. It is further shown that merging through soft collision (from regimes II to I) occurs subsequent to the attainment of maximum deformation and the droplets have started to recede from each other, while merging through hard collision (from regimes II to III) occurs relatively early in the collision process, when the interfaces approach each other.

It is also demonstrated that merging can be effected by using an augmented van der Waals force that compensates for the failure of the present continuum description to bring the colliding interfaces to within the range of molecular attraction. It is emphasized that while such an approach is empirical, the extent of the augmentation is consistent with the difference between the calculated closest distance of approach and the range of the van der Waals force. Furthermore, the satisfactory agreement between the experimental and computed results supports this approach. Indeed, there are many approaches of this nature, in which a macroscopic description of a microscopic phenomenon is enabled through the use of some empirically but self-consistently determined parameter. As such, the potential utility of the augmented Hamaker constant extracted herein in the study of continuum flows affected by surface forces merits further exploration.

ACKNOWLEDGMENTS

The work was supported by the Air Force Office of Scientific Research under the technical monitoring of Dr. M. Birkan. We thank Professors Wei Shyy and G. Tryggvason for helpful discussions.

- ¹Y. J. Jiang, A. Umemura, and C. K. Law, *J. Fluid Mech.* **234**, 171 (1992).
- ²J. Qian and C. K. Law, *J. Fluid Mech.* **331**, 59 (1997).
- ³N. Ashgriz and J. Y. Poo, *J. Fluid Mech.* **221**, 183 (1990).
- ⁴J. R. Adam, N. R. Lindblad, and C. D. Hendricks, *J. Appl. Phys.* **39**, 5173 (1968).
- ⁵P. R. Brazier-Smith, S. G. Jennings, and J. Latham, *Proc. R. Soc. London, Ser. A* **326**, 393 (1972).
- ⁶S. O. Unverdi and G. Tryggvason, *J. Comput. Phys.* **100**, 25 (1992).
- ⁷M. R. Nobari, Y.-J. Jan, and G. Tryggvason, *Phys. Fluids* **8**, 29 (1996).
- ⁸L. P. Chin, Central States Section Meeting of the Combustion Institute, St. Louis, MO, 1996 (unpublished).
- ⁹S. O. Unverdi, "Numerical simulations of multi-fluid flows," Ph.D. thesis, The University of Michigan, 1990.
- ¹⁰K. L. Pan, "Dynamics of droplet collision and flame-front motion," Ph.D. thesis, Princeton University, 2004.
- ¹¹K. L. Pan and C. K. Law, *J. Fluid Mech.* **587**, 1 (2007).
- ¹²H. Lamb, *Hydrodynamics* (Dover, New York, 1932).
- ¹³F. M. White, *Viscous Fluid Flow*, 2nd ed. (McGraw-Hill, New York, 1991).
- ¹⁴S. Middleman, *Modeling Axisymmetric Flows: Dynamics of Films, Jets, and Drops* (Academic, New York, 1995).
- ¹⁵H. C. Hamaker, *Physica* **4**, 1058 (1937).
- ¹⁶A. K. Chesters, *Trans. Inst. Chem. Eng., Part A* **69**, 259 (1991).
- ¹⁷L. M. Hocking, *J. Eng. Math.* **7**, 207 (1973).
- ¹⁸G. Barnocky and R. H. Davis, *J. Colloid Interface Sci.* **121**, 226 (1988).
- ¹⁹R. R. Sundararajakumar and D. L. Koch, *J. Fluid Mech.* **313**, 283 (1996).
- ²⁰G. Barnocky and R. H. Davis, *J. Fluid Mech.* **209**, 501 (1989).
- ²¹H. K. Kytömaa and R. J. Schmid, *Phys. Fluids A* **4**, 2683 (1992).
- ²²A. Gopinath, S. B. Chen, and D. L. Koch, *J. Fluid Mech.* **344**, 245 (1997).
- ²³A. Gopinath and D. L. Koch, *J. Fluid Mech.* **454**, 145 (2002).
- ²⁴R. H. Davis, J. A. Schonberg, and J. M. Rallison, *Phys. Fluids A* **1**, 77 (1989).